Tunneling Effects in Crossed $Ta_2Pt_3Se_8$ – $Ta_2Pd_3Se_8$ Nanoribbon Junctions: Implications for Photodetectors and Circuits

Tianjiao Wang[1], Yanglin Zhu[2], Zhiqiang Mao[2], and Ya-Qiong Xu[,1,3]*

[1]Department of Electrical Engineering and Computer Science, Vanderbilt University, Nashville, TN 37235, USA

[2]Department of Physics, Pennsylvania State University, University Park, PA 16802, USA

[3]Department of Physics and Astronomy, Vanderbilt University, Nashville, TN 37235, USA

[*]Correspondence to: yaqiong.xu@vanderbilt.edu

Abstract

Quasi-one-dimensional van der Waals (vdW) materials are a promising system for future applications in electronics and optoelectronics. Here we report systematic studies on the electronic and optoelectronic properties of crossed junctions composed of two vdW nanoribbons: *p*-type $Ta_2Pt_3Se_8$ (TPtS) and *n*-type $Ta_2Pd_3Se_8$ (TPdS). Asymmetric nonlinear output behaviors are observed in crossed junctions, where a rectifying barrier is formed due to the depletion of majority carriers at the heterointerface with a transmission probability of ~ 0.025. Optoelectronic characteristics reveal inelastic tunneling effects of the crossed junctions. Furthermore, polarized photocurrent measurements demonstrate that isotropic photocurrent signals are detected at the TPtS-TPdS interface, while the maximum photocurrent signals for each nanoribbon are present when the incident light is polarized along the nanoribbon direction. This indicates that photo-excited carriers in both TPtS and TPdS nanoribbons can tunnel through the rectifying barrier at the crossed junction to generate photocurrent signals. Additionally, our photocurrent spectra measurements find that the bandgaps of individual nanoribbons are thickness-dependent and range from 0.9 eV to 1.1 eV, in good agreement with theoretical predictions. These results shed light on the electrical transport and photocurrent generation mechanisms for the nanoscale crossed junctions, opening a door for engineering future vdW materials based electronic and optoelectronic devices, such as point photodetectors and multiterminal circuits.

Keywords: van der Waals materials, tunneling effect, quasi-1D, crossed junction, photocurrent

Introduction

Two-dimensional (2D) van der Waals (vdW) materials have attracted extensive attention since the last century due to the wealth of novel physical properties.[1-3] In the past decade, graphene has been demonstrated to possess remarkable merits for electronics and optoelectronics.[4-7] The great success of graphene inspires researchers to re-discover and re-examine other 2D vdW materials.[1-3, 8] One of the most well-studied 2D vdW material families is transition metal dichalcogenides (TMDCs).[1, 3] The variety of elements and thickness-dependence render TMDCs a wide range of electronic and optoelectronic properties.[9-11] For instance, bulk TMDC crystals possess indirect bandgaps, while monolayer TMDCs become direct-bandgap semiconductors. Their sizeable bandgaps enable TMDCs based field-effect transistors (FETs) with high on/off ratios. Graphene analogues are another important type of 2D vdW materials, which include hexagonal boron nitride (hBN) with a large bandgap up to 6 eV,[12] anisotropic black phosphorus (BP),[8, 13-16] and borophene.[17] 2D vdW materials present several advantages over conventional three-dimensional ones for optoelectronics. First, although the innate thinness renders these materials almost transparent, strong light-matter interactions lead to decent single-pass absorption. For example, monolayer MoS_2 absorbs ~ 10% at excitonic resonances.[18] Moreover, 2D vdW materials cover a wide response spectral range from microwave to ultraviolet wavelengths. For instance, BP, a prospective graphene substitute, shows bandgaps ranging from 0.3 eV in bulk to 2 eV for a monolayer structure, thus allowing BP to be used for broadband optoelectronics. Finally, the absence of dangling bonds makes it easy to stack 2D vdW materials together to form vertical vdW heterostructures, opening up new avenues for engineering electronic and optoelectronic devices with numerous

exciting new functionalities and applications, such as tunneling devices, photodetectors, Light emitting diodes, plasmonic devices, multiterminal circuits and so on.[19-25]

Recently, quasi-one-dimensional (quasi-1D) vdW materials have attracted extensive attention. These materials possess unique chain-like structures bonded by relatively weak inter-chain forces. The examples include the transition metal trichalcogenides MX_3 (M=Ti, Nb, Ta, Zr; X=S, Se, Te), the ternary chalcogenides $M_2X_3Y_8$ (M=Ta, Nb; X=Ni, Pd, Pt; Y=S, Se), and so on.[26] Quasi-1D vdW materials are expected to inherit some features from 2D ones, such as strong light-matter coupling, thickness-dependent bandgaps, and the capability of forming vdW heterostructures. Quasi-1D vdW materials are also expected to own unique thermal, electrical and optical properties due to their distinctive chain structures, including partially ballistic heat transport and high anisotropy ratios in conductivity and optical absorption/emission.[26, 27] For example, partially ballistic phonon transport has been detected in suspended $Ta_2Pd_3Se_8$ (TPdS) nanoribbons that can persist over 13 μm along the chain-axis at room temperature.[27] TiS_3 has been predicted to have electron mobility as high as 10000 $cm^2 \cdot V^{-1} \cdot s^{-1}$ and has demonstrated to own strong electrical and optical anisotropy.[28-31] Exceptionally high breakdown current density and low noise have been observed for $ZrTe_3$ and $TaSe_3$ nanoribbons.[32-34] Furthermore, the bandgaps of these materials range from 0.2 eV to 2.0 eV,[26] making them ideal candidates for high performance FETs and broadband optoelectronics. In particular, ternary chalcogenides TPdS and $Ta_2Pt_3Se_8$ (TPtS) have been predicted to own thickness-dependent bandgaps ranging from 0.525 eV in bulk to 1.038 eV for a single-ribbon structure,[35-37] rendering them promising electronic and optoelectronic materials. More importantly, TPdS nanoribbons appear to be *n*-type

semiconductors, while TPtS nanoribbons show *p*-type behaviors, enabling to form a crossed *p*-*n* junction by stacking them together. Furthermore, two atomically-thin quasi-1D semiconductors are bonded by vdW force with nanoscale confinement. Therefore, interlayer transition and many novel electronic and optoelectronic properties are expected. However, previous studies main focus on the properties of individual TPtS or TPtS nanowires.[38, 39] A comprehensive study for the TPtS/TPtS junction is lacking.

Here we report fabrication, electronic and optoelectronic properties of the nanoscale crossed junctions between perpendicularly stacked *p*-type TPtS and *n*-type TPdS nanoribbons via a vdW transfer technique. Electrical transport measurements reveal that a rectifying barrier is formed in crossed junctions with a transmission probability of ~ 0.025. Further optoelectronic characteristics demonstrate that isotropic photocurrent signals are detected at the TPtS-TPdS heterointerface via inelastic tunneling effects, while polarized photocurrent responses are found in each individual TPtS/TPdS channels, where the maximum photocurrent signals for each nanoribbon are observed when the incident light is polarized along the nanoribbon direction. To clarify the photocurrent generation mechanisms at the nanoscale crossed junctions, wavelength-dependent photocurrent measurements have been performed to explore the bandgaps of individual nanoribbons. Our results have shown that few-layer TPtS/TPdS nanoribbons have thickness-dependent bandgaps that range from 0.9 eV to 1.1 eV, consistent with the previously-reported band structure calculations.[37] These fundamental studies not only develop a strategy to build a nanoscale crossed junction between two quasi-1D vdW materials, but also provide an in-depth understanding on the electrical transport and photocurrent generation mechanisms

for vdW nanoribbons and their nanoscale heterojunctions, offering new design rules for future polarized electronic and optoelectronic devices.

Results and discussion

Figure 1a illustrates the schematic diagram of a typical heterojunction, consisting of a TPdS nanoribbon that is perpendicularly stacked on top of a TPtS nanoribbon and four metal electrodes that are connected to both ends of two nanoribbons, respectively. Here single crystals of TPdS/TPtS were grown using chemical vapor transport shown in Scheme 1. (see details in Supporting Information). Ultrathin TPtS and TPdS nanoribbons were mechanically exfoliated atop a degenerately-doped Si substrate covered with a 280-nm-thick thermal SiO_2 layer, respectively. An optical microscope was used to identify and select thin TPtS/TPdS nanoribbons with their thicknesses ranging from 10 nm to 30 nm.[37] In order to avoid Fermi-level pinning and chemical disorder at metal-nanoribbon interfaces, a vdW transfer technique was adapted to provide clean metal-nanoribbon contacts.[40] Moreover, since the interface quality is expected to influence the tunneling effect of the junction, this transfer technique was further developed to build TPtS-TPdS heterojunctions from freshly cleaved flakes without any chemical treatment and contamination. Briefly, gold electrodes were first prepared on a silicon substrate and then mechanically released from the substrate by a poly(methyl methacrylate) (PMMA) layer and a Polydimethylsiloxane (PDMS) stamp. Next, the released metal electrodes were carefully aligned and placed on top of a TPdS nanoribbon under an optical microscope. The TPdS nanoribbon was then picked up by lifting the PDMS stamp slowly. After that, the PDMS-PMMA-metal-TPdS stack was perpendicularly aligned and physically laminated on top of

a TPtS nanoribbon, subsequently followed by heating and lifting the PDMS stamp. As a result, a PMMA-metal-TPdS-TPtS stack with clean metal-nanoribbon and nanoribbon-nanoribbon interfaces was placed on the SiO_2/Si substrate. Finally, a standard electron-beam lithography process was conducted to remove the PMMA atop contact pads, providing exposed metal pads for subsequent electronic and optoelectronic measurements. The fabrication process steps are shown in Scheme 1. shown in Scheme 1. The inset of Figure 1a presents an optical image of a typical TPtS-TPdS heterojunction. Back-gate voltages were applied to the nanoribbons through a 280 nm SiO_2 layer. Both electronic and optoelectronic properties of the device were characterized in a Janis ST-500 Microscopy Cryostat under high vacuum ($\sim 10^{-6}$ Torr).

Figure 1b displays the gate-dependent characteristics of individual nanoribbons, where TPtS and TPdS nanoribbons show *p*-type and *n*-type behaviors, respectively. The *I-V* characteristics shows that both TPtS and TPdS nanoribbons possess nearly linear output curves at various temperatures (Figure 1c and 1d), indicating nearly ohmic contacts are formed between nanoribbons and metal electrodes. Furthermore, an increase in the conductance is observed for both nanoribbons when the temperature rises from 140 K to 280 K, owing to their semiconductor nature.[41] As illustrated in Figure 1e, the *I-V* characteristics of the TPtS-TPdS junction are subsequently investigated. Non-linear behaviors are observed at various temperatures, suggesting that a rectifying barrier is formed at the TPtS-TPdS interface. Here, few-layer TPtS and TPdS nanoribbons show *p*-type and *n*-type characteristics, respectively. Once they contact with each other, TPtS tends to bend downward while TPdS bends upward to align their Fermi levels, leading to a built-in junction barrier between them as shown in Figure 1e top inset. Forward biases can reduce

the barrier and thus generate a current flow, which extrapolates to a positive intercept at the large-bias linear region and gives a measure of the barrier height of 230 meV at a temperature of 280 K. Reverse biases increase the barrier, while the small depletion region enables tunneling transmission to occur through the barrier, leading to a measurable current flow that increases with increasing reverse bias. In addition to the junction barrier between two nanoribbons, charge carriers have to pass one depletion region in the TPtS nanoribbon and the other depletion region in the TPdS nanoribbon. The transmission probability (T_d) for each depletion region can be estimated from the transmission probability ($T_S \approx T_d^2$) along each nanoribbon, where the depletion region needs to be passed twice (insets of Figure 1c,d).[42] Here, the electrons in the n-type TPdS nanoribbon can flow to the p-type TPtS nanoribbons through the middle contact region. Similarly, the holes can transport from TPtS to TPdS. As a result, the middle region of the TPdS/TPtS nanoribbon is depleted and bended upwardly/downwardly. Ts can be calculated from the conductance of each ribbon: $T_S = G/(4e^2/h)$, where e is the electron charge and h is Planck's constant. Therefore, the transmission probability can be given by $T_{TPtS\text{-}TPdS} \approx T_{d\_TPtS} \cdot T_j \cdot T_{d\_TPdS}$., where T_j is the tunneling transmission probability at the heterointerface between TPtS and TPdS nanoribbons. On the other hand, $T_{TPtS\text{-}TPdS}$ can also be calculated from the junction conductance at low-bias linear region ($V_{ds} < \pm 50$ mV) (Figure 1e bottom inset). As a result, T_j can be estimated to be around 0.025 (for another device, Tj is 0.059), suggesting that a charge carrier arriving at the heterointerface has chance of a few percent of tunneling from TPtS to TPdS nanoribbons. This is similar to the transmission probability previously reported for the vdW force bonded single-walled carbon nanotubes ($T_j \sim 0.02$ to 0.06).[42]

To further explore the tunneling transmission at the TPtS-TPdS junction, the optoelectronic properties of the heterojunctions were investigated using scanning photocurrent microscopy under various drain-source voltages. Here a continuous wave laser beam (NKT Photonics SuperK Supercontinuum Laser) was expanded and then focused by a 40X Olympus objective (N.A. = 0.6) into a diffraction-limited spot (~1 μm), which scanned over the device by a piezo-controlled mirror with nanometer-scale spatial resolution. Photocurrent signals ($I_{pc} = I_{laser} - I_{dark}$) were recorded as a function of position, resulting in a spatially resolved photocurrent map of the device. The reflection of the incident laser beam was simultaneously recorded to locate the position of the sample. Figure 2a shows a photocurrent image of the TPtS-TPdS junction, where the TPtS/TPdS nanoribbon and metal electrodes are outlined by pink/blue and gold dashed lines, respectively. Strong photocurrent responses are observed at the TPtS-TPdS junction, where the potential barrier is formed due to Fermi level alignment, leading to a built-in electric field that can separate photo-excited electron-hole pairs (EHPs) to generate photocurrents. The red/blue color represents a positive/negative current, where the positive current indicates the current flows from the drain to source electrode (Figure 2b). Under a back-gate voltage of -80 V and a zero bias, negative photocurrent signals are detected in the junction region, which is consistent with the negative short circuit current for conventional *p-n* junctions via photovoltaics effect (PVE) as shown in Figure 2c middle.[43] If a forward bias is applied, the built-in electric field can be partially cancelled or the total electrostatic potential can be reduced, making it difficult to separate the photo-excited EHPs (Figure 2c right). Under this circumstance, inelastic/elastic-tunneling-mediated-interlayer recombination may compete with photo-excited carries separation/collection, leading to

negligible photocurrent responses. Here the interlayer recombination could be related to Shockley-Read-Hall recombination, where majority carriers can be trapped in the intragap states, or Langevin recombination through the Coulomb interaction, or a combination of both.[44] On the other hand, a reverse bias (V_{ds} = -1V) raises the total electrostatic potential and thus facilitate the separation of the photo-excited EHPs. Therefore, the photo-excited carries are quickly separated and then collected by electrodes before the interlayer recombination recombined at the heterointerface, leading to enhanced photocurrent signals (Figure 2c left). We note that the photoconductive effect is also very important for the photocurrent generation. However, the nonlinear photocurrent bias dependency of the TPtS-TPdS junction suggests that the photoconductive effect may not be the major contribution to the photocurrent generation.[45]

To clarify the photocurrent generation mechanisms at the nanoscale crossed junctions, polarization-dependent photocurrent measurements have been performed to explore individual nanoribbons and their heterojunctions. Figure 3a shows a photocurrent image of the *p*-type TPtS nanoribbon, where the nanoribbon and metal electrodes are outlined by pink and gold dashed lines, respectively. Strong photocurrent responses are observed at the nanoribbon-metal interfaces, where potential barriers are formed due to Fermi level alignment, leading to built-in electric fields that can separate photo-excited electron-hole pairs (EHPs) to generate photocurrents. The red/blue color represents a positive/negative current, where the positive current indicates the current flows from the drain to source electrode. For the *p*-type TPtS nanoribbon, since the electronic energies are lower near the contacts than those in the middle of the nanoribbon, electrons will flow from the middle channel to electrodes (Figure 1c inset), resulting in a positive/negative

current flow at the drain/source electrode. When a drain-source bias of 5V is applied, the intensity of the positive photocurrent response at the drain electrode is strongly enhanced. We have also found that the photocurrent response of the TPtS nanoribbon is anisotropic. As shown in Figure 3b, the photocurrent signals are maximized when the incident light is polarized along the TPtS nanoribbon direction (or 0°). The direction of the polarization is defined as shown in Figure 3a, where 0° and 90° denote the directions parallel to the TPtS and TPdS nanoribbons, respectively. The polarized effect likely arises from the unique chain-like structure of TPtS nanoribbons, giving the quasi-1D properties to these nanoribbons. As a result, a smaller part of the incident light is expected to be coupled into the nanoribbons for the cross-polarized light, leading to anisotropic optical absorption, as reported in other 1D or quasi-1D structures.[29, 30, 46-49] The anisotropic photoresponse of TPtS nanoribbons opens another degree of freedom in development of future polarized optoelectronics.

Similarly, an opposite polarity of photocurrent responses is observed for the *n*-type TPdS nanoribbon at the nanoribbon-metal interfaces (Figure 3c), where the electronic energies are higher near the contacts than in the middle of the nanoribbon (Figure 1d inset), leading to a flow of electrons from the electrodes to the middle channel or negative/positive photocurrent signals near the drain/source electrode. We note that slight photocurrent can also be detected along the TPdS nanowire, which may be related to the small bending of the top TPdS nanowire.[39] As we expected, the maximum photocurrent response of the TPdS nanoribbon occurs for the light polarization direction parallel to the nanoribbon (90 °C) (Figure 3d). Furthermore, we explore the polarized optoelectronic properties of the TPtS-TPdS junction. As shown in Figure 3e, the majority of photocurrent signals are

detected in the overlap region between TPtS and TPdS nanoribbons, where the built-in electric field can efficiently separate the photo-excited EHPs to generate photocurrent responses (Figure 1e top inset). Interestingly, the photocurrent signals observed at the TPtS-TPdS junction show nearly isotropic behavior (Figure 3f), suggesting photo-excited EHPs in both nanoribbons contribute to the photocurrent generation in the junction region. The entire TPtS-TPdS system provides an ideal candidate for controllable polarized photodetection.

By varying the wavelength of the incident light, we explored the spectral response of individual TPtS and TPdS nanoribbons. Figure 4 shows the measured normalized photocurrent signals as a function of the light wavelength (P = 80 μW) for TPtS/TPdS nanoribbons with different thicknesses. We could roughly estimate the bandgaps of nanoribbons by extracting the cut-off wavelength of photoresponsivity.[50] A thinner TPtS nanoribbon that shows relatively light color under an optical microscope (Figure 4a) tends to have a larger band gap of 1.08 eV (1150 nm), while the thicker one (Figure 4b) owns a band gap of 0.99 eV (1250 nm). Similarly, the bandgaps for TPdS nanoribbons are 1.03 eV (1200 nm) and 0.92 eV (1350 nm), respectively. This is in good agreement with the previous electronic band structure calculations, which predict that the bandgaps of TPtS/TPdS are thickness-dependent and there is a transition from 1.038 eV in a single-layer structure to 0.525 eV in bulk material.[37] More accurate measurements of the nanoribbon thickness/width and other bandgap characteristics are required in the future to pin down the relationship between the bandgap and size of TPtS/TPdS nanoribbons.

Conclusion

In summary, we report nanoscale crossed junctions between perpendicularly stacked *p*-type TPtS and *n*-type TPdS nanoribbons. Asymmetric nonlinear output behaviors are observed in crossed junctions, where a rectifying barrier is formed due to the depletion of majority carriers at the heterointerface with a transmission probability of ~ 0.025. Subsequent optoelectronic characteristics reveal that inelastic tunneling effects are detected in crossed junctions. Moreover, isotropic photocurrent signals are observed at the nanoscale TPtS-TPdS heterojunction, while TPtS/TPdS nanoribbons exhibit polarized photoresponses, suggesting that the photocurrent signals at the heterojunctions are likely attributed to photo-excited carriers in both TPtS and TPdS nanoribbons. Bias-dependent photocurrent measurements further demonstrate that the photocurrent generation at the TPtS-TPdS crossed junction primarily stems from the PVE, which is similar to conventional *p*-*n* junctions. With the assistance of the photoresponse spectra of TPtS/TPdS nanoribbons, their bandgaps can be estimated to be around 0.9 eV to 1.1 eV and depend on their thickness, consistent to previous theoretical predications. These studies not only offer a way to build nanoscale junctions, but also provide fundamental understandings on the electronic and optoelectronic properties of vdW nanoribbons and their heterojunctions, opening up new avenues for engineering point photodetectors, multiterminal circuits and future anisotropic electronics and optoelectronics.

Methods

TPdS/TPtS crystal growth

Single crystals of TPdS/TPtS were grown using chemical vapor transport. The mixture of thoroughly ground stoichiometric Ta, Pd and Se element powders was loaded

into a quartz tube and sealed under vacuum. The tube with loaded materials was pre-heated for a week at 750 °C. The obtained powder was then ground again and transferred to a new quartz tube (inside diameter = 0.9 cm) together with 75 mg iodine as transport agent. The tube was vacuumed and sealed at the point 15 cm away from charge end and then put into a double zone furnace. The charge end and the other end were heated to 850 °C and 900 °C respectively. After holding for one day, the temperature was reversed with charge end at 900 °C and cold end at 850°C. The furnace was shut down after one week. Long needle-like crystals (up to a few centimeters) with silver luster formed at the cold end. Preliminary composition analyses on different crystals using Energy Dispersive X-ray Spectrometer showed the ratio of Ta, Pd/Pt, and Se atoms very close to 2:3:8. The powder X-ray diffraction at room temperature confirmed the phase to be TPdS/TPtS. Furthermore, structure of these nanowires was then determined by comparing annular dark-field scanning transmission electron microscope (ADF-STEM) images with the simulated atomic structure images.

Acknowledgment

This work was supported by the National Science Foundation (ECCS-1810088 and CBET-1805924) and Vanderbilt Discovery Grant. Financial support for sample preparation was provided by the National Science Foundation through the Penn State 2D Crystal Consortium-Materials Innovation Platform (2DCC-MIP) under NSF cooperative agreement DMR-1539916.

Additional information

The authors declare no competing financial interests.

Scheme 1

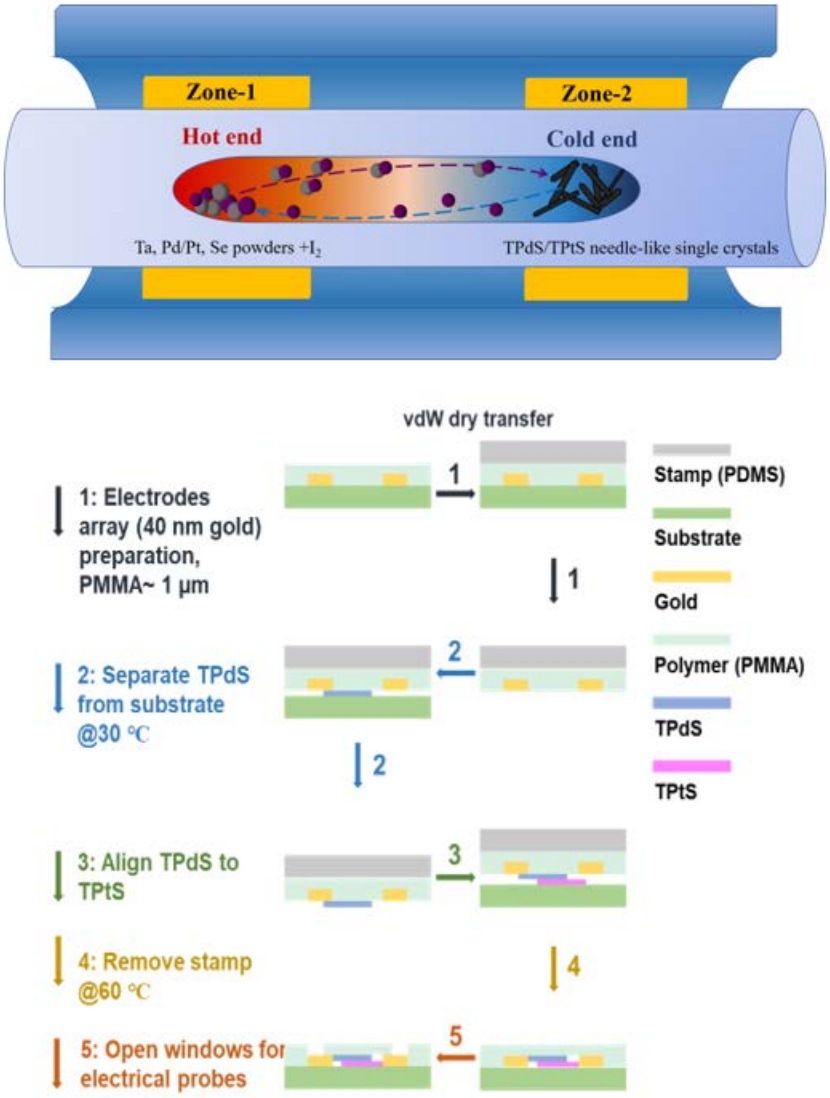

Scheme of the chemical vapor transport for the TPdS/TPtS crystal growth and vdW dry transfer for the device fabrication.

Figures

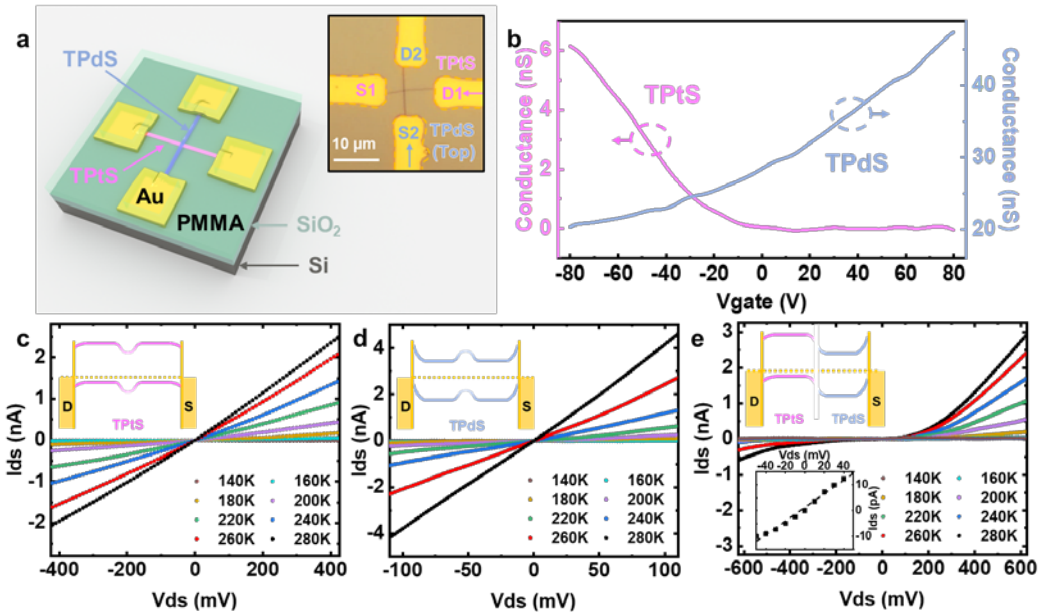

Figure 1. (a) A schematic diagram of a nanoscale crossed junction between perpendicularly stacked TPtS and TPdS nanoribbons. Inset: optical micrograph of a typical device. S and D indicate source and drain electrodes, respectively. The gold dashed lines mark the edges of metal electrodes. (b) Gate-dependent characteristics for TPtS and TPdS nanoribbons based FETs. I_{ds}-V_{ds} characteristics and band diagrams of (c) the TPtS nanoribbon with a gate voltage of -80 V and (d) the TPdS nanoribbon with a gate voltage of 80 V at various temperatures. (e) I_{ds}-V_{ds} characteristics of the TPtS-TPdS junction with a gate voltage of -80 V at various temperatures. Inset: the band diagram of the TPtS-TPdS junction (top) and the low-bias region & its linear fitting (down).

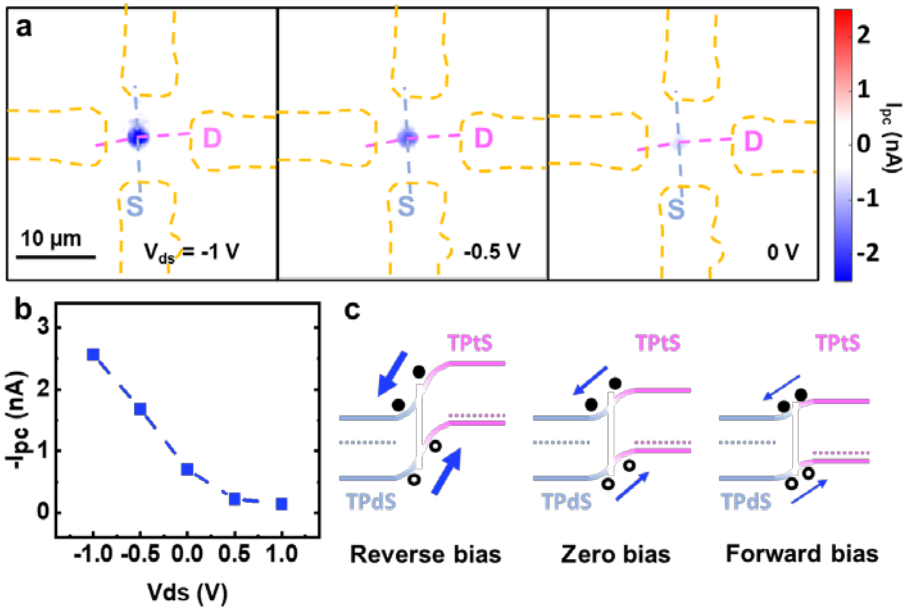

Figure 2. (a) Scanning photocurrent images of the TPtS-TPdS junction under different drain-source biases. (b) Intensities of photocurrent signals in the junction region when the drain-source voltage sweeps from -1 V to 1 V with a step of 0.5 V. (c) Band diagrams for the TPtS-TPdS junction under different biases.

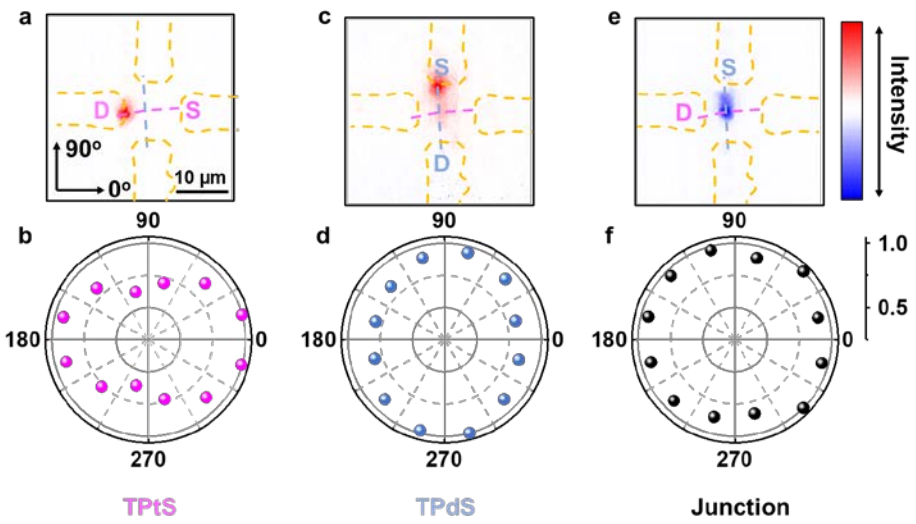

Figure 3. Scanning photocurrent images of (a) the TPtS FET (+5V bias), (c) the TPdS FET (+1V bias), and (e) the TPtS-TPdS junction (+5V bias), respectively. Normalized photocurrent intensities as a function of the incident light polarization direction for (b) the TPtS FET, (d) the TPdS FET, and (f) the TPtS-TPdS heterojunction, respectively.

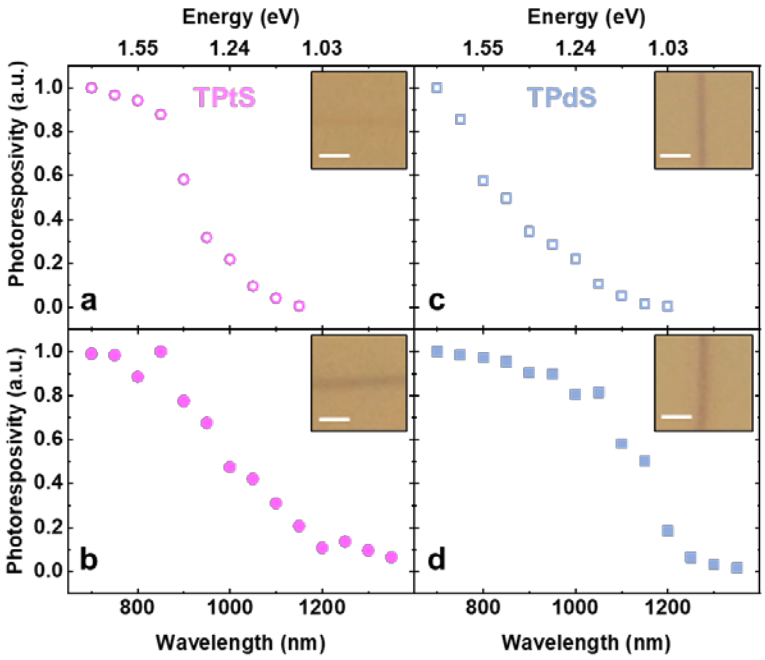

Figure 4. Photocurrent signals measured as a function of the incident light wavelength for TPtS (a and b) and TPdS (c and d) nanoribbons with different thicknesses. Inset: optical images of TPtS/TPdS nanoribbons. The scale bars are 1 μm.

References

(1) Mak, K. F.; Shan, J., Photonics and optoelectronics of 2D semiconductor transition metal dichalcogenides. *Nature Photonics* **2016,** *10* (4), 216-226.
(2) Akinwande, D.; Brennan, C. J.; Bunch, J. S.; Egberts, P.; Felts, J. R.; Gao, H.; Huang, R.; Kim, J.-S.; Li, T.; Li, Y.; Liechti, K. M.; Lu, N.; Park, H. S.; Reed, E. J.; Wang, P.; Yakobson, B. I.; Zhang, T.; Zhang, Y.-W.; Zhou, Y.; Zhu, Y., A review on mechanics and mechanical properties of 2D materials—Graphene and beyond. *Extreme Mechanics Letters* **2017,** *13*, 42-77.
(3) Wang, Q. H.; Kalantar-Zadeh, K.; Kis, A.; Coleman, J. N.; Strano, M. S., Electronics and optoelectronics of two-dimensional transition metal dichalcogenides. *Nature Nanotechnology* **2012,** *7* (11), 699-712.
(4) Schwierz, F., Graphene transistors. *Nature Nanotechnology* **2010,** *5* (7), 487-496.
(5) Zhang, B. Y.; Liu, T.; Meng, B.; Li, X.; Liang, G.; Hu, X.; Wang, Q. J., Broadband high photoresponse from pure monolayer graphene photodetector. *Nature Communications* **2013,** *4*, 1811.
(6) Xia, F.; Mueller, T.; Lin, Y.-m.; Valdes-Garcia, A.; Avouris, P., Ultrafast graphene photodetector. *Nature Nanotechnology* **2009,** *4* (12), 839-843.
(7) Bonaccorso, F.; Sun, Z.; Hasan, T.; Ferrari, A. C., Graphene photonics and optoelectronics. *Nature Photonics* **2010,** *4* (9), 611-622.
(8) Xia, F.; Wang, H.; Jia, Y., Rediscovering black phosphorus as an anisotropic layered material for optoelectronics and electronics. *Nature Communications* **2014,** *5*.
(9) RadisavljevicB; RadenovicA; BrivioJ; GiacomettiV; KisA, Single-layer MoS_2 transistors. *Nature Nanotechnology* **2011,** *6* (3), 147-150.
(10) Ross, J. S.; Klement, P.; Jones, A. M.; Ghimire, N. J.; Yan, J.; Mandrus, D. G.; Taniguchi, T.; Watanabe, K.; Kitamura, K.; Yao, W.; Cobden, D. H.; Xu, X., Electrically tunable excitonic light-emitting diodes based on monolayer WSe_2 p-n junctions. *Nature Nanotechnology* **2014,** *9* (4), 268-272.
(11) Lopez-Sanchez, O.; Lembke, D.; Kayci, M.; Radenovic, A.; Kis, A., Ultrasensitive photodetectors based on monolayer MoS2. *Nature Nanotechnology* **2013,** *8* (7), 497-501.
(12) Shi, Y.; Hamsen, C.; Jia, X.; Kim, K. K.; Reina, A.; Hofmann, M.; Hsu, A. L.; Zhang, K.; Li, H.; Juang, Z.-Y.; Dresselhaus, M. S.; Li, L.-J.; Kong, J., Synthesis of Few-Layer Hexagonal Boron Nitride Thin Film by Chemical Vapor Deposition. *Nano Letters* **2010,** *10* (10), 4134-4139.
(13) Li, L. K.; Yu, Y. J.; Ye, G. J.; Ge, Q. Q.; Ou, X. D.; Wu, H.; Feng, D. L.; Chen, X. H.; Zhang, Y. B., Black phosphorus field-effect transistors. *Nature Nanotechnology* **2014,** *9* (5), 372-377.
(14) Buscema, M.; Groenendijk, D. J.; Blanter, S. I.; Steele, G. A.; van der Zant, H. S. J.; Castellanos-Gomez, A., Fast and Broadband Photoresponse of Few-Layer Black Phosphorus Field-Effect Transistors. *Nano Letters* **2014,** *14* (6), 3347-3352.
(15) Hong, T.; Chamlagain, B.; Lin, W.; Chuang, H.-J.; Pan, M.; Zhou, Z.; Xu, Y.-Q., Polarized photocurrent response in black phosphorus field-effect transistors. *Nanoscale* **2014,** *6* (15), 8978-8983.
(16) Liu, H.; Neal, A. T.; Zhu, Z.; Luo, Z.; Xu, X.; Tománek, D.; Ye, P. D., Phosphorene: An Unexplored 2D Semiconductor with a High Hole Mobility. *ACS Nano* **2014,** *8* (4), 4033-4041.

(17) Mannix, A. J.; Zhou, X.-F.; Kiraly, B.; Wood, J. D.; Alducin, D.; Myers, B. D.; Liu, X.; Fisher, B. L.; Santiago, U.; Guest, J. R.; Yacaman, M. J.; Ponce, A.; Oganov, A. R.; Hersam, M. C.; Guisinger, N. P., Synthesis of borophenes: Anisotropic, two-dimensional boron polymorphs. *Science* **2015,** *350* (6267), 1513-1516.
(18) Eda, G.; Maier, S. A., Two-Dimensional Crystals: Managing Light for Optoelectronics. *Acs Nano* **2013,** *7* (7), 5660-5665.
(19) Geim, A. K.; Grigorieva, I. V., Van der Waals heterostructures. *Nature* **2013,** *499* (7459), 419-425.
(20) Novoselov, K. S.; Mishchenko, A.; Carvalho, A.; Castro Neto, A. H., 2D materials and van der Waals heterostructures. *Science* **2016,** *353* (6298), aac9439.
(21) Withers, F.; Del Pozo-Zamudio, O.; Mishchenko, A.; Rooney, A. P.; Gholinia, A.; Watanabe, K.; Taniguchi, T.; Haigh, S. J.; Geim, A. K.; Tartakovskii, A. I.; Novoselov, K. S., Light-emitting diodes by band-structure engineering in van der Waals heterostructures. *Natural Materials* **2015,** *14* (3), 301-306.
(22) Liu, Y.; Weiss, N. O.; Duan, X.; Cheng, H.-C.; Huang, Y.; Duan, X., Van der Waals heterostructures and devices. *Nature Reviews Materials* **2016,** *1*, 16042.
(23) Fang, H.; Battaglia, C.; Carraro, C.; Nemsak, S.; Ozdol, B.; Kang, J. S.; Bechtel, H. A.; Desai, S. B.; Kronast, F.; Unal, A. A.; Conti, G.; Conlon, C.; Palsson, G. K.; Martin, M. C.; Minor, A. M.; Fadley, C. S.; Yablonovitch, E.; Maboudian, R.; Javey, A., Strong interlayer coupling in van der Waals heterostructures built from single-layer chalcogenides. *Proceedings of the National Academy of Sciences* **2014,** *111* (17), 6198-6202.
(24) Lv, Q.; Yan, F.; Wei, X.; Wang, K., High-Performance, Self-Driven Photodetector Based on Graphene Sandwiched GaSe/WS2 Heterojunction. *Advanced Optical Materials* **2018,** *6* (2), 1700490.
(25) Lv, Q.; Yan, F.; Mori, N.; Zhu, W.; Hu, C.; Kudrynskyi, Z. R.; Kovalyuk, Z. D.; Patanè, A.; Wang, K., Interlayer Band-to-Band Tunneling and Negative Differential Resistance in van der Waals BP/InSe Field-Effect Transistors. *Advanced Functional Materials* **2020,** *30* (15), 1910713.
(26) Island, J. O.; Molina-Mendoza, A. J.; Barawi, M.; Biele, R.; Flores, E.; Clamagirand, J. M.; Ares, J. R.; Sánchez, C.; van der Zant, H. S. J.; D'Agosta, R.; Ferrer, I. J.; Castellanos-Gomez, A., Electronics and optoelectronics of quasi-1D layered transition metal trichalcogenides. *2D Materials* **2017,** *4* (2), 022003.
(27) Zhang, Q.; Liu, C.; Liu, X.; Liu, J.; Cui, Z.; Zhang, Y.; Yang, L.; Zhao, Y.; Xu, T. T.; Chen, Y.; Wei, J.; Mao, Z.; Li, D., Thermal Transport in Quasi-1D van der Waals Crystal Ta2Pd3Se8 Nanowires: Size and Length Dependence. *ACS Nano* **2018,** *12* (3), 2634-2642.
(28) Dai, J.; Zeng, X. C., Titanium trisulfide monolayer: theoretical prediction of a new direct-gap semiconductor with high and anisotropic carrier mobility. *Angew Chem Int Ed Engl* **2015,** *54* (26), 7572-6.
(29) Jin, Y.; Li, X.; Yang, J., Single layer of MX3 (M = Ti, Zr; X = S, Se, Te): a new platform for nano-electronics and optics. *Physical Chemistry Chemical Physics* **2015,** *17* (28), 18665-18669.
(30) Island, J. O.; Biele, R.; Barawi, M.; Clamagirand, J. M.; Ares, J. R.; Sánchez, C.; van der Zant, H. S. J.; Ferrer, I. J.; D'Agosta, R.; Castellanos-Gomez, A., Titanium

trisulfide (TiS3): a 2D semiconductor with quasi-1D optical and electronic properties. *Scientific Reports* **2016,** *6*, 22214.
(31) Lipatov, A.; Wilson, P. M.; Shekhirev, M.; Teeter, J. D.; Netusil, R.; Sinitskii, A., Few-layered titanium trisulfide (TiS3) field-effect transistors. *Nanoscale* **2015,** *7* (29), 12291-12296.
(32) Geremew, A.; Bloodgood, M. A.; Aytan, E.; Woo, B. W. K.; Corber, S. R.; Liu, G.; Bozhilov, K.; Salguero, T. T.; Rumyantsev, S.; Rao, M. P.; Balandin, A. A., Current Carrying Capacity of Quasi-1D ZrTe3Van Der Waals Nanoribbons. *IEEE Electron Device Letters* **2018,** *39* (5), 735-738.
(33) Liu, G.; Rumyantsev, S.; Bloodgood, M. A.; Salguero, T. T.; Shur, M.; Balandin, A. A., Low-Frequency Electronic Noise in Quasi-1D TaSe3 van der Waals Nanowires. *Nano Letters* **2017,** *17* (1), 377-383.
(34) Stolyarov, M. A.; Liu, G.; Bloodgood, M. A.; Aytan, E.; Jiang, C.; Samnakay, R.; Salguero, T. T.; Nika, D. L.; Rumyantsev, S. L.; Shur, M. S.; Bozhilov, K. N.; Balandin, A. A., Breakdown current density in h-BN-capped quasi-1D TaSe3 metallic nanowires: prospects of interconnect applications. *Nanoscale* **2016,** *8* (34), 15774-15782.
(35) Keszler, D. A.; Ibers, J. A.; Maoyu, S.; Jiaxi, L., New ternary and quaternary transition-metal selenides: Syntheses and characterization. *Journal of Solid State Chemistry* **1985,** *57* (1), 68-81.
(36) Keszler, D. A.; Ibers, J. A., A new structural type in ternary chalcogenide chemistry: Structure and properties of Nb2Pd3Se8. *Journal of Solid State Chemistry* **1984,** *52* (1), 73-79.
(37) Liu, X.; Liu, J.; Antipina, L. Y.; Hu, J.; Yue, C.; Sanchez, A. M.; Sorokin, P. B.; Mao, Z.; Wei, J., Direct Fabrication of Functional Ultrathin Single-Crystal Nanowires from Quasi-One-Dimensional van der Waals Crystals. *Nano Letters* **2016,** *16* (10), 6188-6195.
(38) Liu, X.; Liu, S.; Antipina, L. Y.; Zhu, Y.; Ning, J.; Liu, J.; Yue, C.; Joshy, A.; Zhu, Y.; Sun, J.; Sanchez, A. M.; Sorokin, P. B.; Mao, Z.; Xiong, Q.; Wei, J., High yield production of ultrathin fibroid semiconducting nanowire of Ta2Pd3Se8. *Nano Research* **2020,** *13* (6), 1627-1635.
(39) Sukhanova, E. V.; Sorokin, P. B., Specific Response of the Atomic and Electronic Structure of Ta2Pd3Se8 and Ta2Pt3Se8 Nanoribbons to the Uniaxial Strain. *The Journal of Physical Chemistry C* **2020,** *124* (13), 7539-7543.
(40) Liu, Y.; Guo, J.; Zhu, E.; Liao, L.; Lee, S.-J.; Ding, M.; Shakir, I.; Gambin, V.; Huang, Y.; Duan, X., Approaching the Schottky–Mott limit in van der Waals metal–semiconductor junctions. *Nature* **2018,** *557* (7707), 696-700.
(41) Singh, A.; Philipose, U., Understanding the Mechanisms that Affect the Quality of Electrochemically Grown Semiconducting Nanowires. 2018.
(42) Fuhrer, M. S.; Nygård, J.; Shih, L.; Forero, M.; Yoon, Y.-G.; Mazzoni, M. S. C.; Choi, H. J.; Ihm, J.; Louie, S. G.; Zettl, A.; McEuen, P. L., Crossed Nanotube Junctions. *Science* **2000,** *288* (5465), 494-497.
(43) Lin, C.; Wang, B.; Teo, K.; Zhang, Z., Performance comparison between photovoltaic and thermoradiative devices. *Journal of Applied Physics* **2017,** *122*, 243103.
(44) Lee, C.-H.; Lee, G.-H.; van der Zande, A. M.; Chen, W.; Li, Y.; Han, M.; Cui, X.; Arefe, G.; Nuckolls, C.; Heinz, T. F.; Guo, J.; Hone, J.; Kim, P., Atomically thin p–n junctions with van der Waals heterointerfaces. *Nature Nanotechnology* **2014,** *9* (9), 676-681.

(45) Tsen, A. W.; Donev, L. A. K.; Kurt, H.; Herman, L. H.; Park, J., Imaging the electrical conductance of individual carbon nanotubes with photothermal current microscopy. *Nature Nanotechnology* **2009,** *4* (2), 108-113.
(46) Pant, A.; Torun, E.; Chen, B.; Bhat, S.; Fan, X.; Wu, K.; Wright, D. P.; Peeters, F. M.; Soignard, E.; Sahin, H.; Tongay, S., Strong dichroic emission in the pseudo one dimensional material ZrS3. *Nanoscale* **2016,** *8* (36), 16259-16265.
(47) Wu, K.; Torun, E.; Sahin, H.; Chen, B.; Fan, X.; Pant, A.; Parsons Wright, D.; Aoki, T.; Peeters, F. M.; Soignard, E.; Tongay, S., Unusual lattice vibration characteristics in whiskers of the pseudo-one-dimensional titanium trisulfide TiS3. *Nature Communications* **2016,** *7*, 12952.
(48) Nanot, S.; Cummings, A. W.; Pint, C. L.; Ikeuchi, A.; Akiho, T.; Sueoka, K.; Hauge, R. H.; Léonard, F.; Kono, J., Broadband, Polarization-Sensitive Photodetector Based on Optically-Thick Films of Macroscopically Long, Dense, and Aligned Carbon Nanotubes. *Scientific Reports* **2013,** *3*, 1335.
(49) Zhang, Y. J.; Ideue, T.; Onga, M.; Qin, F.; Suzuki, R.; Zak, A.; Tenne, R.; Smet, J. H.; Iwasa, Y., Enhanced intrinsic photovoltaic effect in tungsten disulfide nanotubes. *Nature* **2019,** *570* (7761), 349-353.
(50) Zanatta, A. R., Revisiting the optical bandgap of semiconductors and the proposal of a unified methodology to its determination. *Scientific Reports* **2019,** *9* (1), 11225.